Front. Chem. Sci. Eng. 2020, 14(6): 1006–1017
https://doi.org/10.1007/s11705-020-1924-y

RESEARCH ARTICLE

Immobilization of nano-zero-valent irons by carboxylated cellulose nanocrystals for wastewater remediation

Bangxian Peng[1*], Rusen Zhou[2*], Ying Chen[1], Song Tu[1], Yingwu Yin[1], Liyi Ye (✉)[1]

1 Department of Chemical and Biochemical Engineering, College of Chemistry and Chemical Engineering, Xiamen University, Xiamen 361005, China

2 School of Chemistry, Physics and Mechanical Engineering, Queensland University of Technology, Brisbane, QLD 4000, Australia

Abstract Nano-zero-valent irons (nZVI) have shown great potential to function as universal and low-cost magnetic adsorbents. Yet, the rapid agglomeration and easy surface corrosion of nZVI in solution greatly hinders their overall applicability. Here, carboxylated cellulose nanocrystals (CCNC), widely available from renewable biomass resources, were prepared and applied for the immobilization of nZVI. In doing so, carboxylated cellulose nanocrystals supporting nano-zero-valent irons (CCNC-nZVI) were obtained via an *in-situ* growth method. The CCNC-nZVI were characterized and then evaluated for their performances in wastewater treatment. The results obtained show that nZVI nanoparticles could attach to the carboxyl and hydroxyl groups of CCNC, and well disperse on the CCNC surface with a size of ~10 nm. With the CCNC acting as corrosion inhibitors improving the reaction activity of nZVI, CCNC-nZVI exhibited an improved dispersion stability and electron utilization efficacy. The Pb(II) adsorption capacity of CCNC-nZVI reached 509.3 $mg \cdot g^{-1}$ (298.15 K, pH = 4.0), significantly higher than that of CCNC. The adsorption was a spontaneous exothermic process and could be perfectly fitted by the pseudo-second-order kinetics model. This study may provide a novel and green method for immobilizing magnetic nanomaterials by using biomass-based resources to develop effective bio-adsorbents for wastewater decontamination.

Keywords carboxylated cellulose nanocrystals, nano-zero-valent irons, magnetic bio-adsorbents, wastewater remediation

1 Introduction

The remediation of wastewater that often contains heavy metals (Pb, Cd, Cr, etc.) and/or organic compounds with significant environmental and physiological toxicity, represents a great challenge facing this modern society [1–4]. Efficient, economical and sustainable solutions toward water purification are now urgently required due to the severe water pollution and the generally higher standards set on water quality [5–7]. Among various techniques (membrane separation [5], electrochemical precipitation [6], advanced oxidation processes [7], etc.) developed for waste removal, degradation or detoxification of water contaminants, adsorption represents a traditional but simple method exhibiting high efficacy and wide applicability [1,7]. To further demonstrate the power of adsorption treatment and improve the associated benefits, designing and developing novel and low-cost adsorbents in order to further enhance adsorption efficiency is of great significance.

The Nano-zero-valent irons (nZVI), a type of iron-based materials, have attracted significant interests in the scientific community due to high iron source availability, low toxicity, high reactivity and attractive magnetic properties, which may help simplify the following procedures after adsorption [8]. As an effective reducing agent, nZVI are able to achieve both pollutant adsorption and reduction (or oxidation by inducing reactive oxygen species (ROS) generated in aqueous solution), and have been successfully applied to remove various contaminants including heavy metal ions [9], organic compounds [10], dyes and textile compounds [11]. Due to the high activity, the surface of nZVI is often covered with a porous oxide film. Therefore, it may be difficult for pollutants to pass directly through the pores of the oxide film into the surface of nZVI for subsequent reduction. Meanwhile, adsorption and co-precipitation are mainly happened on the surface

Received November 7, 2019; accepted January 24, 2020

E-mail: lyye@xmu.edu.cn

*These authors contributed equally to this work.

oxide film to capture metal and metalloid pollutants, which renders nZVI attractive to be used as adsorbents in wastewater treatment [12]. However, the use of nZVI in adsorption applications is often challenged by rapid agglomeration (poor dispersity) and significant surface corrosion of the nanoparticles, as well as low particle utilization efficiency [13,14]. To solve these general limitations and in order to avoid potential toxicity of the nanoparticles once released into aquatic environments, the use of solid substrates to support or immobilize the nZVI may offer a suitable method for the use in wastewater remediation [9,11]. The search for ideal support materials or stabilizers for improving the applicability and durability of nZVI-based adsorbents has been of major research interest, especially with encouraging results obtained by using bentonite [15], chitosan [16], biochar [17], carboxymethyl cellulose [18], or multiwalled carbon nanotubes [19] as supporting materials.

Cellulose, widely available from renewable biomass resources, is the most abundant organic polymer on the planet and represents a promising raw material for different processing purposes due to its low cost, high strength, good biocompatibility and controllable surface chemistry [20]. Natural cellulose can be degraded via chemical, mechanical and enzymatic methods to extract cellulose nanocrystals (CNC) [21,22]. Because of the reduction in physical size and the enhancement in specific surface area, CNC has been demonstrated to be suitable as a green stabilizer for metal nanoparticles, such as TiO_2 [23], Fe_2O_3 [24], silver [25] and gold [26]. With CNC, nanoparticles can be stabilized on the surface of CNC, with the coagulation/agglomeration significantly reduced and the dispersity and reactivity considerably enhanced [23–26]. In addition, CNC can be easily modified or functionalized by ways of oxidation [27], esterification [28], silylation [29] and/or polymer grafting [30] to render the material more multifunctional, which may then further equip CNC with suitable characteristics for immobilizing nanomaterials.

In this study, we prepared CCNC through an efficient one-step hydrolytic oxidation of microcrystalline cellulose in a mixed acid system. To the best of our knowledge, this is the first time the as-obtained CCNC was used for the immobilization of nZVI, which was achieved via an *in-situ* reduction method and provided composites, termed CCNC supporting nZVI (CCNC-nZVI), as shown in Scheme 1. The structure and chemical properties of CCNC-nZVI were characterized and compared with pristine nZVI. To evaluate the efficacy of CCNC-nZVI used as adsorbents, adsorption experiments on commonly used simulated wastewater samples as well as the mechanism of the adsorption process were studied and discussed.

2 Experimental

2.1 Materials

Microcrystalline cellulose (MCC), NaOH (analytical reagent (AR)), $FeSO_4 \cdot 7H_2O$ (AR), KBH_4 (97 wt-%), ethanol (AR), H_2SO_4 (98 wt-%), HCl (37 wt-%), and HNO_3 (68 wt-%) were purchased from Sinopharm Chemical Reagent Co., Ltd. (Shanghai, China). $Pb(NO_3)_2$ (99 wt-%) was purchased from Xilong Chemical Industry Co., Ltd. (Guangdong, China). All chemicals were dissolved in deionized water and used as received without further purification.

2.2 Synthesis of composite adsorbents

The preparation of CCNC was carried out according to a method previously reported by Cheng et al. with some minor modifications [27]. CCNC was simultaneously hydrolyzed and oxidized from MCC (2 g) by using 120 mL of mixed acid consisting of HCl and HNO_3 (volume ratio of 7:3) at 110°C for 3h. The suspension was diluted with ultra-pure water (18.2 $M\Omega \cdot cm^{-1}$) and centrifuged three times to remove any remaining acid. The suspension was then dialyzed with cellulose dialysis membranes with a cutoff molecular weight of 12–14 kDa against ultra-pure water until the suspension pH was neutral. The solution was then freeze-dried for 48 hours to obtain the CCNC solid particles.

CCNC-nZVI were synthesized through liquid phase reduction of $FeSO_4 \cdot 7H_2O$ using KBH_4. CCNC (0.1 g) and $FeSO_4 \cdot 7H_2O$ (0.496 g) were dissolved in 100 mL ultra-

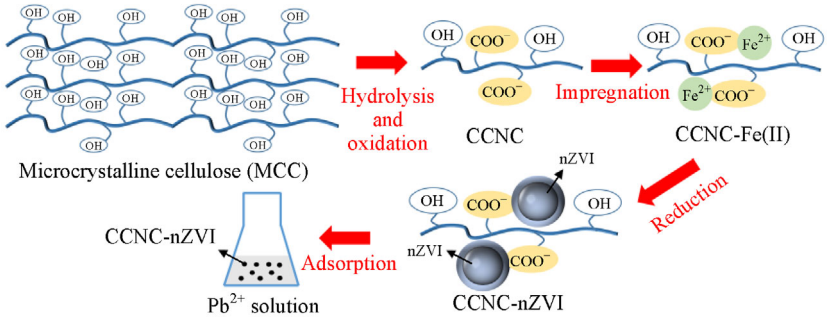

Scheme 1 Diagram highlighting the preparation process of CCNC-nZVI and the application as absorbents for Pb(II) removal.

pure water through an ultrasonic dispersion method. Next, KBH_4 (0.482 g) solution was added dropwise to the mixture (approximately 5 $mL \cdot min^{-1}$) under agitation until no further production of H_2 bubbles could be observed. The entire reaction mixture was flushed with N_2 to ensure inert non-oxidative conditions. After magnetic separation, the obtained composite samples were washed and purified by deoxygenated water and ethanol for three times, respectively. The composites were then vacuum-dried at 60°C for 12 h. The iron reduction equation can be described as follows:

$$2Fe^{2+} + BH_4^- + 4H_2O \rightarrow$$

$$2Fe^0 \downarrow + B(OH)_4^- + 4H^+ + 2H_2 \uparrow \quad (1)$$

2.3 Characterization of composite materials

The morphological properties of the samples were analyzed using scanning electron microscopy (SEM, Hitachi, S-4800, Japan) and transmission electron microscopy (TEM, JEOL, JEM-2100, Japan). The crystal structure and crystallinity were analyzed on a powder X-ray diffractometer (XRD, Rigaku Ultima IV, Japan) operating at 40 kV and 30 mA with Cu Kα radiation. The surface functional groups were evaluated using Fourier transform infrared spectroscopy (FTIR, 7300-200CM, USA). The particle size distribution and zeta potential of the sample suspensions were investigated using a Malvern Nano-ZS90 Zetasizer. The total contents of Pb and Fe in solution were detected using flame atomic adsorption spectrophotometry (VARIAN AA 240FS, America). The magnetic hysteresis loops were measured using a vibrating sample magnetometer (VSM, Lake Shore 7404, USA). X-ray photoelectron spectroscopy (XPS, Thermo Escalab 250Xi, USA) was used to reveal the electron binding energy of samples before and after adsorption.

2.4 Batch experiments for Pb(II) removal

Batch adsorption experiments were performed in 150 mL conical flacks using a digital constant temperature shaker (150 $r \cdot min^{-1}$). Pure nZVI (20 mg) or CCNC-nZVI with different mass ratios of CCNC and nZVI (20 mg) were added to 50 mL of 100 $mg \cdot L^{-1}$ Pb(II) solution, respectively. The effects of pH on the removal process were studied by regulating the initial pH from 2.0 to 8.0 using 0.1 $mol \cdot L^{-1}$ HNO_3 or NaOH solutions. Pb(II) solutions (50 mL each) at concentrations of 50, 100, 150, 200, 250 or 300 $mg \cdot L^{-1}$ were obtained from a standard stock solution. The solution pH was adjusted to 4.0 and the samples were then mixed with 20 mg of CCNC-nZVI for studying the influences of the initial concentration and the adsorption isotherms (detailed in Electronic Supplementary Material, ESM). The adsorbents and Pb(II) solutions were mixed and allowed to react for different reaction times (up to 4 h) so as to determine the adsorption equilibrium time and to investigate the adsorption kinetics (also detailed in ESM). After adsorption, the adsorbents and solutions were separated by adding a magnet. Remaining metals in the solutions were then quantified by atomic adsorption spectrophotometry after being filtered through 0.22 μm filters.

The removal rate R (%) and equilibrium adsorption capacity q_e ($mg \cdot g^{-1}$) were calculated by Eqs. (2) and (3) as follows:

$$R = \frac{C_0 - C_e}{C_0} \times 100\%, \quad (2)$$

$$q_e = \frac{V(C_0 - C_e)}{m}, \quad (3)$$

where C_0 and C_e are the initial and equilibrium concentrations of Pb(II) ($mg \cdot L^{-1}$) in solution, respectively. V is the adsorbate volume (mL) and m is the adsorbent mass (g). Each adsorption experiment was repeated at least three times and an average was calculated and used to assess the adsorption efficacy.

3 Results and discussion

3.1 Morphologies and properties of CCNC

The morphologies of the as-prepared CCNC were investigated by SEM and TEM as shown in Figs. 1(a) and 1(b). Most CCNC were in the form of rod-like crystals with lengths ranging from 80 to 250 nm. As can be seen from the SEM images, the CCNC were densely distributed, presumably due to the surface tension of water when dried on the silicon wafer. Peaks at 15.0°, 22.6° and 34.2° in the XRD patterns of CCNC (Fig. 1(c)) were observed, corresponding to the typical cellulose I-type crystal planes of (110), (200) and (004) [27]. The Zeta potential was determined to reflect the dispersion stability of the colloids. The transformation of surface hydroxyl groups to carboxyl groups could render the surface of CCNC more negatively charged. As expected, the CCNC suspension featured a negative Zeta potential value, regardless of the initial pH, and the absolute values gradually rose with the increase of pH (Fig. 1(d)). After ultrasonic treatment of the solutions at pH = 7, a moderately stable CCNC solution could be obtained. Considering that a higher pH leads to precipitation formation (metal hydroxides, e.g., $Fe(OH)_2$), the CCNC suspension was dialyzed at a pH of 7 in all subsequent experiments. As displayed in Fig. 1(d), the diameter distribution of accumulated crystals indicated that about 80% of the nanocrystals exhibited an average diameter of 130±70 nm. In order to provide information on the effects of carboxyl groups, the cellulose nanocrys-

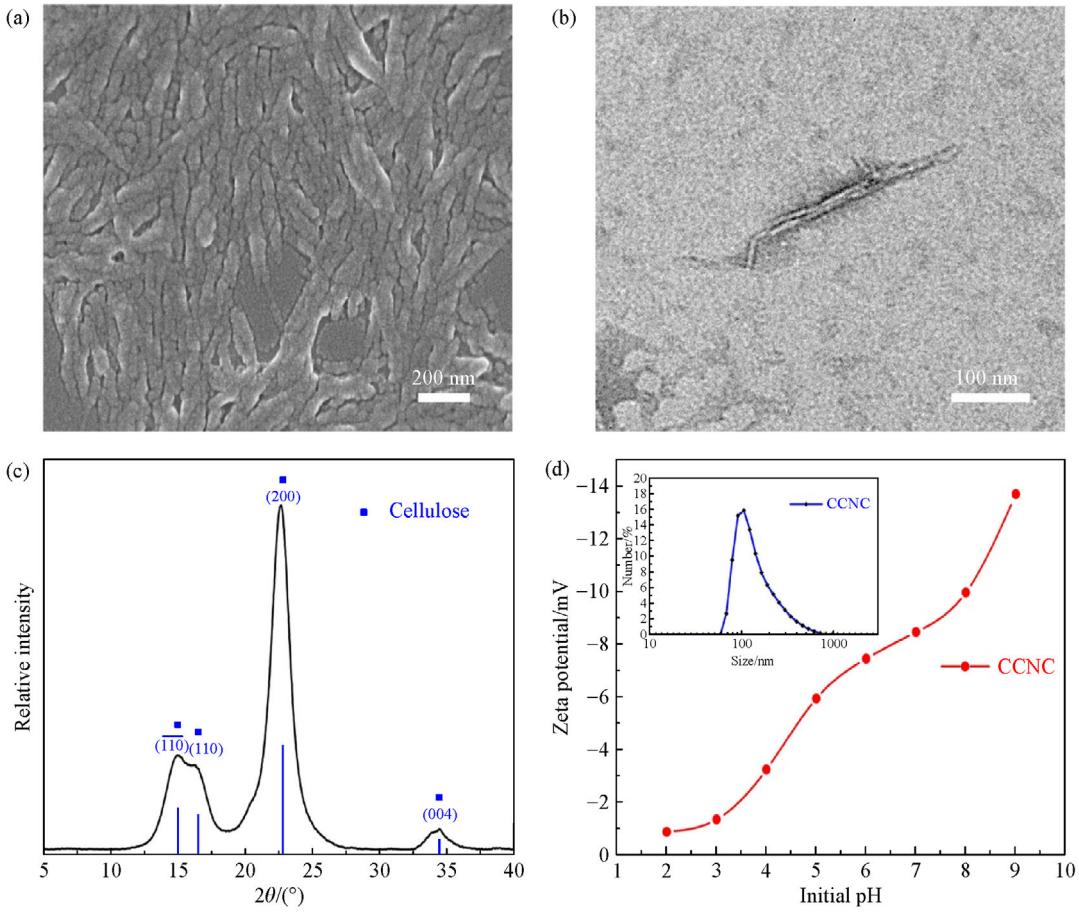

Fig. 1 (a) SEM, (b) TEM, (c) XRD characterization of CCNC, and (d) the Zeta potential of CCNC (inset shows the size distribution of CCNC at pH = 7).

tals (CNC) were prepared using hydrochloric acid alone, and the physical appearances of CNC and CCNC in aqueous solution were compared as shown in Figs. S1(a) and S1(b) (cf. ESM). The colour of the CCNC suspension was light blue without clear precipitation, which showed a clear Tyndall effect. CCNC in suspension could be stored under ambient conditions for over one month proving their stability. However, clear stratification could be observed in the case of CNC immediately after solution preparation. The results indicated that electrostatic repulsion among CCNC particles was the reason for reducing the particle agglomeration, enhancing the fluidity in solution and beneficial to the formation of composite materials.

3.2 Characterization of CCNC-nZVI composites

The FTIR spectra of MCC, CCNC, nZVI and CCNC-nZVI at a scanning range of 400–4000 cm^{-1} are illustrated in Fig. 2(a). The broad absorption band at around 3348 cm^{-1} and the absorbance peak at 2901 cm^{-1} corresponded to the stretching vibration of –OH and stretching vibration of C–H, respectively [24]. The peak located at 1112 cm^{-1} could be ascribed to the C–O and the C–O–C stretching vibration of the glucose ring skeleton [27]. It could be seen from the comparison of MCC and CCNC that the –OH stretching vibration was weakened and narrowed after acid hydrolysis, a finding that could be attributed to the reduction of intermolecular and intramolecular hydrogen bonds. Additionally, a new peak at 1731 cm^{-1} appeared in the spectrum of CCNC, corresponding to the characteristic peak of C = O. This finding indicated that more carboxyl groups were introduced on the surface of CCNC due to the oxidization reaction after addition of nitric acid [31]. Furthermore, the spectrum of CCNC-nZVI contained all characteristic peaks corresponding to CCNC and nZVI, while singals in the range of 570–640 cm^{-1} could be attributed to the formation of FeOOH and FeO [32]. As shown in the XRD patterns (Fig. 2(b)), the diffraction peak of pristine nZVI at 44.6° could be attributed to the (110) crystal faces of α-Fe^0 [33]. Two clear diffraction peaks were assigned to CCNC (110) and zero-valent irons (110) were observed in CCNC-nZVI, again indicating the successful formation of CCNC-nZVI composites. After Pb(II) adsorbed, the diffraction peak of nZVI disappeared,

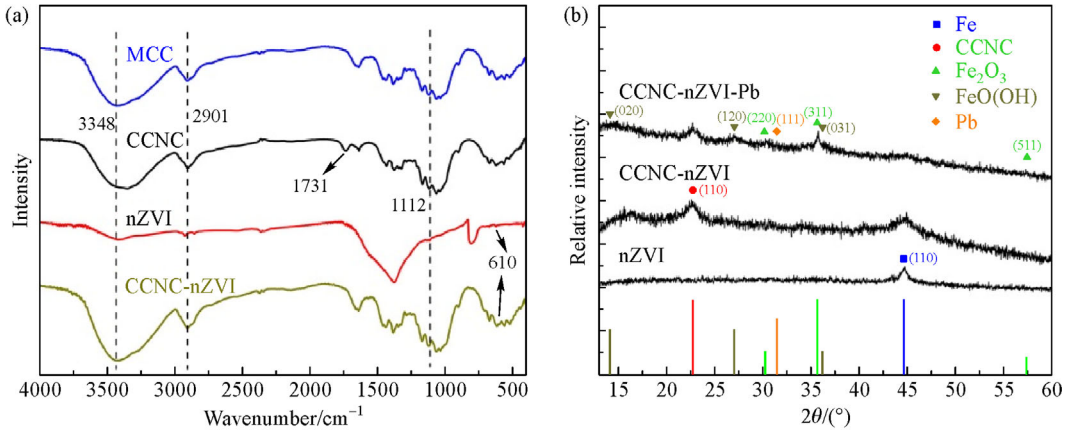

Fig. 2 (a) FTIR spectra of MCC, CCNC, nZVI and CCNC-nZVI; (b) XRD patterns of nZVI, CCNC-nZVI before and after Pb(II) adsorption (CCNC-nZVI-Pb).

however, the Fe_2O_3 peaks (35.7°, 30.3° and 57.4°) and FeO(OH) peaks (14.2°, 27.1° and 36.2°) appeared on the surface. The small peak observed at 31.5°, corresponding to Pb (111) in Pb(II)-adsorbed CCNC-nZVI, confirmed that the Pb(II) ions were indeed reduced.

As shown in Figs. 3(a) and 3(c), the pristine nZVI were mainly determined to be in spherical form with a size of 50–100 nm. Moreover, nZVI was found to aggregate into formless chains due to the magnetic force and electrostatic interactions within the nanoparticles [34]. In the case of CCNC-nZVI (Figs. 3(b) and 3(d)), the sphericity of nZVI was well retained and the nZVI particles were evenly dispersed on the surface of CCNC. The latter was found to form porous structures in CCNC-nZVI, advantageous for inhibiting corrosion effects. The TEM images (Fig. 3(d)) and the particle size distribution (Fig. 3(e)) indicated that the size of nZVI was reduced from ~200 to ~10 nm after immobilization on CCNC, further confirming the good dispersity of nZVI supported by CCNC. Similar results were also obtained from hydraulic diameter (DH) distribution measurements of the nZVI and CCNC-nZVI derived from laser diffraction particle size analysis (Fig. S2, cf. ESM). Due to rapid aggregation of the magnetic nanoparticles, the DH of the nZVI increased up to 500–700 nm, while that of CCNC-nZVI mainly stayed constant at 200 nm. Furthermore, the nano-spheres were shown to be anchored discretely to the carboxyl groups on the surface of CCNC and formed a thermodynamically more stable nanostructure. Moreover, as can be seen from inspection of Fig. 3(f), the BET surface area of CCNC-nZVI increased to 23.43 $m^2 \cdot g^{-1}$, a 3-time increase compared to that of nZVI. The magnetic hysteresis loops of both nZVI and CCNC-nZVI were also measured and the corresponding results were shown in Fig. 3(g). The saturation magnetization reached 147.50 $emu \cdot g^{-1}$ for nZVI and 72.52 $emu \cdot g^{-1}$ for CCNC-nZVI, respectively, indicating that both nZVI and CCNC-nZVI exhibited suitable magnetic properties for the suggested applications. Afterwards, the dispersity and stability of the as-synthesized nZVI and CCNC-nZVI in aqueous media were compared after storage for a certain period of time (Fig. 3(h)). The CCNC-nZVI composites generally presented an improved dispersity, enhancing the transportation of electrons or even ions and thus favoring the adsorption process [21]. It is also worth mentioning in this context that pristine nZVI almost completely corroded after 72 h of storage, while the as-synthesized CCNC-nZVI featured an excellent corrosion inhibition performance, ultimately improving the stability of the composites when used as adsorbents in aqueous solutions.

3.3 Performances of Pb(II) removal over CCNC-nZVI composites

3.3.1 Bath adsorption experiments

The effect of the mass ratio of both CCNC and nZVI present in the CCNC-nZVI composites on the adsorption of Pb(II) is shown in Fig. 4(a). The removal of Pb(II) increased rapidly during the first 30 min and then gradually reached an adsorption equilibrium within 2 h, except in the case of a ratio of 3:1 where an equilibrium was not achieved even after 4 h. Moreover, CCNC-nZVI was shown to effectively remove Pb(II) even with a small amount of iron, yet only 15% of Pb(II) ions were found to be removed by the individual CCNC. This result suggested that an increase on Pb(II) removal could be attributed to the loading of nZVI particles. Meanwhile, the removal rate of CCNC-nZVI (2:1) and CCNC-nZVI (3:1) was found to be lower than that of CCNC-nZVI (1:1), presumably due to the lack of iron content. However, an increase in the nZVI load would not always favor the removal process. For example, the removal performance was found to be less effective in the group of 1:2 than in the 1:1 group. Two possible reasons for this result could be identified: (1) the

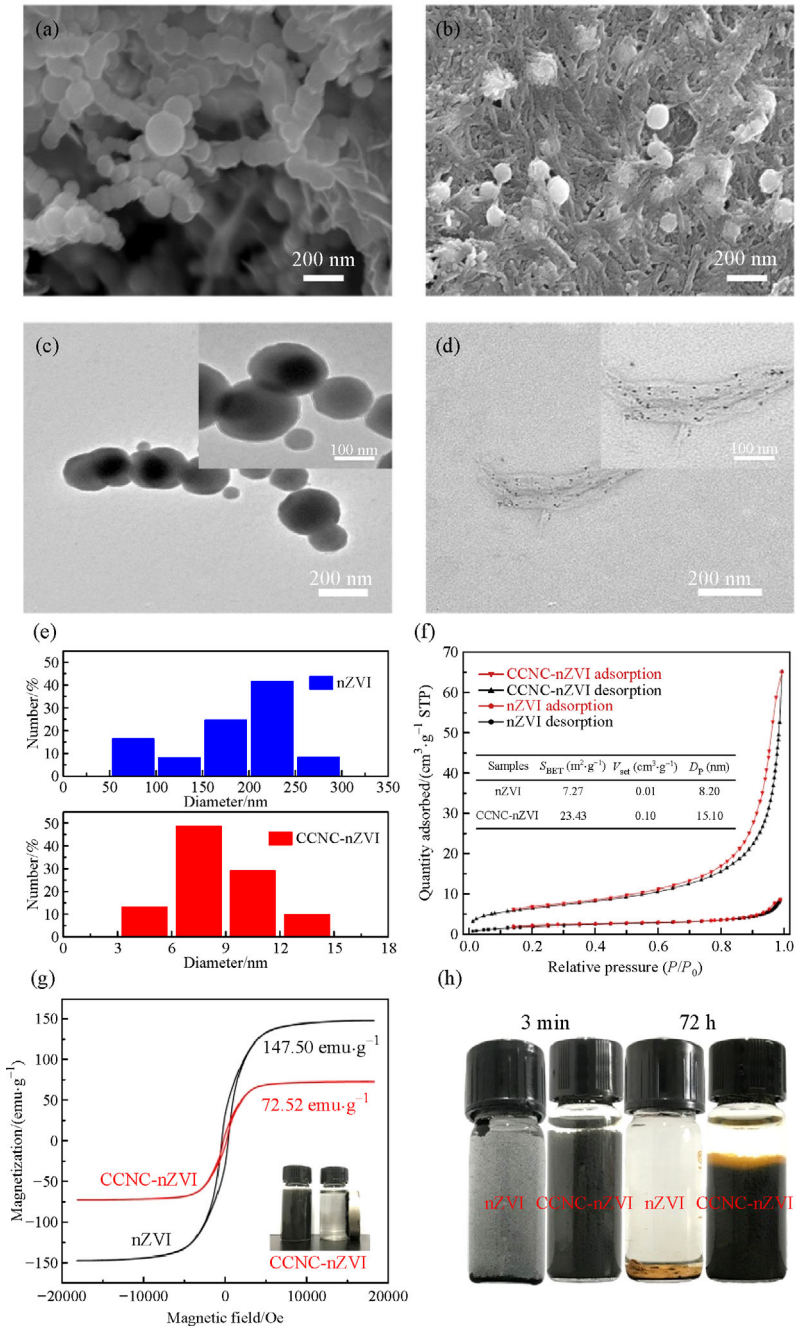

Fig. 3 SEM images of (a) nZVI and (b) CCNC-nZVI; TEM images of (c) nZVI and (d) CCNC-nZVI; (e) size distribution and (f) N_2 adsorption/desorption isotherms of nZVI and CCNC-nZVI; (g) VSM curves of nZVI and CCNC-nZVI and (h) photographs of nZVI and CNCC-nZVI in aqueous solutions for a certain time after synthesized (3 min and 72 h).

uniform dispersion of nZVI particles decreased and the nanoparticles aggregated to form larger particles, thus leading to a reduction of surface area and active sites; (2) the nZVI particles were exposed to the solution in an excessive manner and reacted with H^+, thus resulting in a decrease of electron utilization. Studies on the release of Fe(III) into the nZVI-treated solutions were then conducted in an effort to show that the oxidation-reduction of nZVI would result in both Pb(II) removal and Fe(III) dissolution [35]. As demonstrated in Fig. 4(b), pristine nZVI (without CCNC supported) released 3.469 mg of iron ions after adsorption, which far exceeded the values for CCNC-nZVI (1:3) and CCNC-nZVI (1:1) (1.743 and 1.139 mg, respectively). Furthermore, negatively charged carboxyl and hydroxyl groups present on the surface of CCNC could also adsorb and complex Fe(III)-ions with a

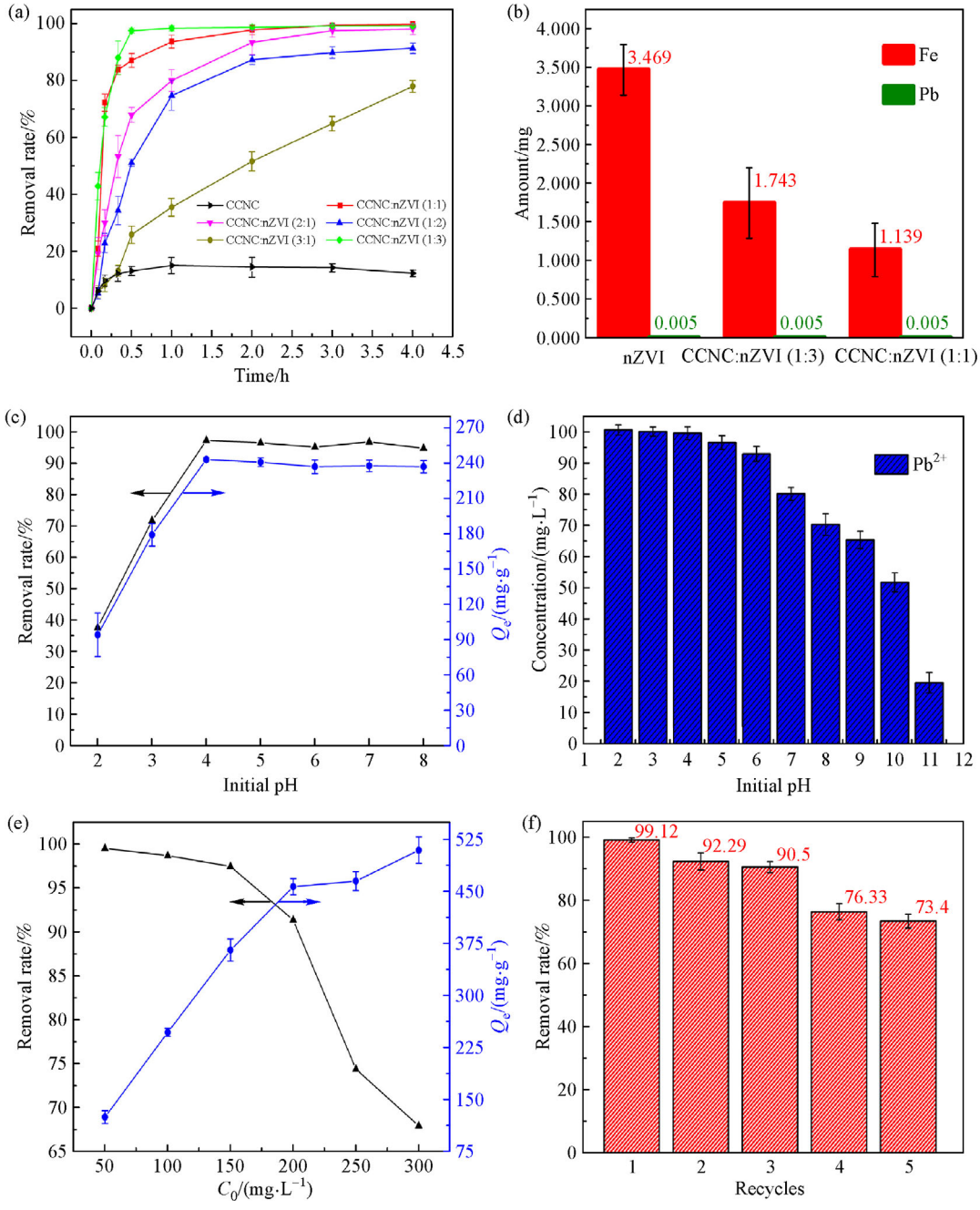

Fig. 4 (a) Effects of adsorption time and mass ratio of CCNC and nZVI in the CCNC-nZVI composites on Pb(II) adsorption capacity, (b) residual content of iron and lead in solutions after adsorption for 2 h, (c) effect of initial pH on adsorption and (d) Pb(II) content, (e) effect of initial concentration on Pb(II) adsorption of CCNC-nZVI (1:1) and (f) regeneration experiment of CCNC-nZVI (1:1).

saturated adsorption capacity toward Fe(III) reaching about 100 mg·g^{-1} (Fig. S3, cf. ESM), further demonstrating that CCNC was able to reduce any unwanted secondary pollution from the release of iron ions [36]. These results revealed that CCNC could reduce the nZVI dissolution and improve the utilization efficacy of electrons of composite adsorbents. Considering the high removal efficiency and in an effort to reduce cost, CCNC-nZVI with a CCNC and nZVI mass ratio of 1:1 were selected for subsequent studies. Figure 4(c) shows the effect of pH on Pb(II) adsorption in a pH range of 2.0 to 8.0. As presented, the reaction of H^+ with nZVI particles resulted in a significantly lower Pb(II) adsorption capacity at pH = 2 or 3. Furthermore, the surface of CCNC was found to be protonated in acidic media and the electrostatic repulsion with positively charged Pb(II) may weaken the adsorption efficacy [37]. In addition, the content of Pb(II) gradually decreased and resulted in precipitation of $Pb(OH)_2$ as the

pH increased (Fig. 4(d)). To avoid the formation of $Pb(OH)_2$ precipitates, the most suitable pH was determined to be about 4. Figure 4(e) exhibits a chart showing the adsorption capacity as a function of initial Pb(II) solution concentration. With an increase in concentration (50–300 $mg \cdot L^{-1}$), the CCNC-nZVI adsorption capacity increased gradually and achieved an astonishing value of 509.3 $mg \cdot g^{-1}$ when the initial concentration was 300 $mg \cdot L^{-1}$. To evaluate the reusability of the particles, the Pb(II) adsorbed composite was first washed three times with oxygen-free ethanol, followed by dissolution in 0.01 $mol \cdot L^{-1}$ hydrochloric acid and addition of 0.05 $mol \cdot L^{-1}$ KHB_4. After regeneration, adsorption of Pb(II) was conducted again with results shown in Fig. 4(f). It was found that the removal efficiency for Pb(II) remained steady (removal > 90%) after being re-used for 3 times and the removal rate still reached 73.4% after 5 cycles, demonstrating a suitable recycling-usability of CCNC-nZVI.

3.3.2 Adsorption kinetics, isotherms and thermodynamic studies

The descriptions of adsorption kinetics, isotherms and thermodynamic studies are presented in the supporting information section (cf. ESM). The kinetic fitting results are shown in Figs. 5(a) and 5(b), with the obtained parameters listed in Table 1. As shown here, a high fitting degree (R^2 = 0.999) with the pseudo-second-order kinetic model implies that the adsorption process was dominated by chemisorption control. Correspondingly, the Zeta potential of CCNC-nZVI reached −18.8 mV (Fig. S4, cf. ESM), suggesting a strong electrostatic attraction between the negative surface of CCNC-nZVI and Pb(II). Therefore, it could be implied that Pb(II) was rapidly adhered to the surface of the adsorbent and complexed with the hydroxyl and carboxyl groups first through electrostatic attraction. Then, Pb(II) underwent intraparticle diffusion and was reduced with nZVI until reaching an adsorption equilibrium. As shown in Figs. 5(c) and 5(d) and listed in Table 2, the adsorption could be well fitted with the Langmuir model and better matched the Freundlich model at 318.15 K, indicating that the monolayer adsorption dominated at low temperatures, with the adsorption gradually changing into the multilayer adsorption with increasing temperatures [38]. Additionally, maximum adsorption capacities of 653.59, 581.40 and 505.05 $mg \cdot g^{-1}$, corresponding to

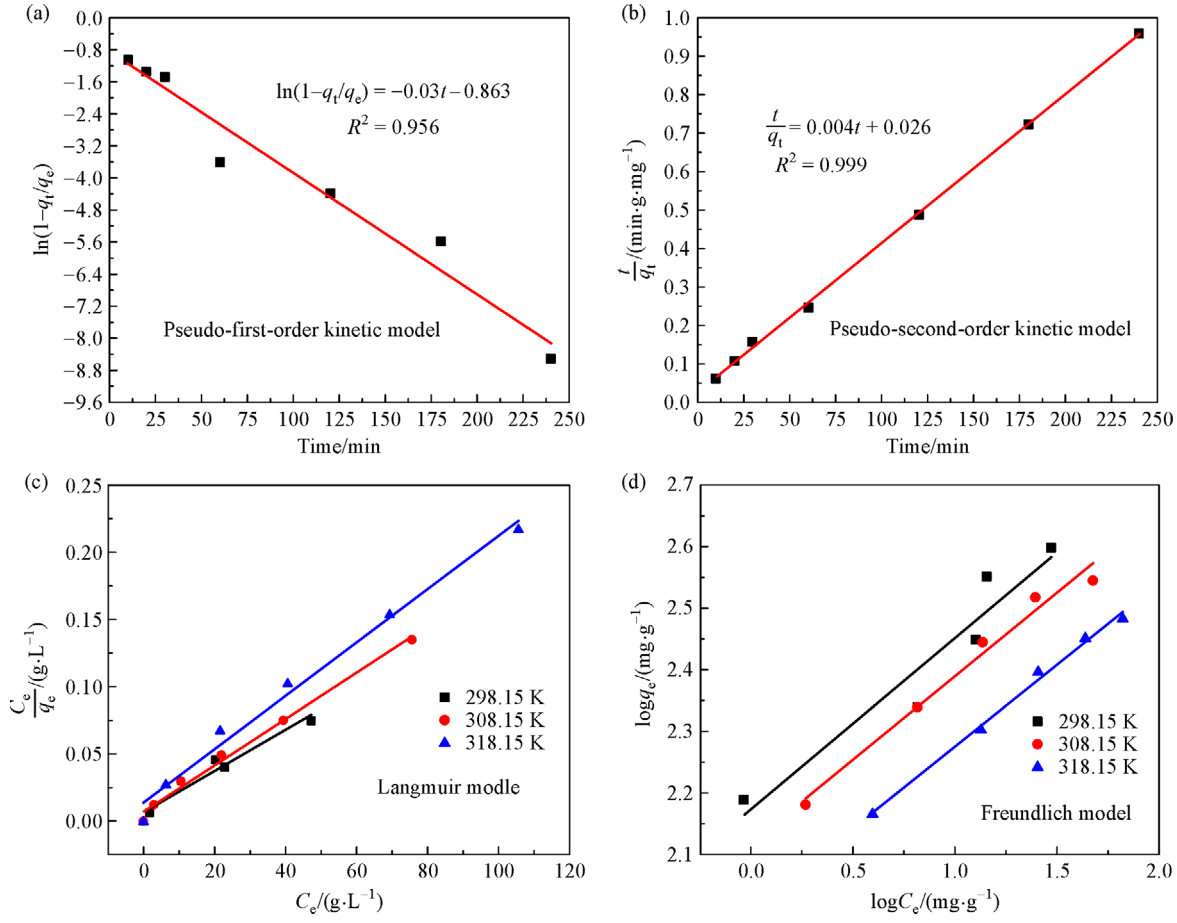

Fig. 5 (a) Pseudo-first-order and (b) pseudo-second-order kinetic models for adsorption (m = 0.4 $g \cdot L^{-1}$, C_0 = 100 $mg \cdot L^{-1}$, pH = 4.0, temperature = 298.15 K); (c) Langmuir and (d) Freundlich isothermal models for adsorption at various temperatures (m = 0.4 $g \cdot L^{-1}$, pH = 4.0).

temperatures of 298.15, 308.15 and 318.15 K were achieved from the Langmuir model. A comparison of the CCNC-nZVI and several adsorbents reported for Pb(II) adsorption was summarized in Table 3. This comparison further highlights the excellent adsorption performance of CCNC-nZVI and demonstrates that CCNC-nZVI exhibit promising characteristics to be developed as effective adsorbents in future applications. The negative Gibbs free energy (listed in Table S1, cf. ESM) also indicates that the adsorption was a spontaneous process. Moreover, ΔG had an obvious correlation with temperature, indicating that the spontaneity of adsorption was gradually weakened as temperature increased. The negative values of ΔH and ΔS further revealed that the adsorption of Pb(II) ion was also an exothermic and entropy reducing process.

3.4 Adsorption mechanism for Pb(II) removal

XPS analysis was carried out to identify the changes on the chemical valence states of the adsorbents CCNC-nZVI before and after adsorption. As can be seen from Fig. 6(a), the presence of Pb 4f clearly confirmed adsorption of Pb (II) on CCNC-nZVI. The high-resolution spectrum of Pb 4f (Fig. 6(b)) on the Pb(II)-loaded adsorbent was fitted with two peaks at 138.6 and 143.5 eV, corresponding to Pb^0 and the complexes of Pb(II), respectively. PbO and $Pb(OH)_2$ would constitute the main components of the Pb(II) precipitates, and the presence of Pb^0 demonstrated a complete reduction process. As shown in Fig. 6(c), the separate peaks located at 709.4, 709.9 and 711.7 eV could be assigned to the binding energies of $2p_{3/2}$ for Fe 2p, indicating that the surface of the supported nZVI mainly consisted of Fe(II) and Fe(III), while a relatively weak peak at 706.2 eV, corresponding to Fe^0 ($2p_{3/2}$) [46], was also found. However, the signal corresponding to Fe^0 disappeared after Pb(II) adsorbed (Fig. 6(d)), suggesting that Fe^0 present on the surface was mainly oxidized and played an important role in the Pb(II) removal process. It should also be noted that internal Fe^0 could not be observed because XPS analysis exhibits a maximum surface probing depth of 2–5 nm. In addition, the results showed that the area of the peak at 711.5 eV (44.81%), corresponding to FeOOH [47], was higher than that before adsorption (20.8%). Presumably, this could be used as evidence that the iron oxidation layer could act as an adsorption layer. A study conducted by Noubactep also showed that the corrosion of zero-valent iron was accompanied with a covering layer of a porous oxide

Table 1 Kinetic parameters for Pb(II) adsorption on CCNC-nZVI

Pseudo-first order			Pseudo-second order		
q_e /(mg·g^{-1})	k_1	R^2	q_e /(mg·g^{-1})	k_2	R^2
249.75	–0.03	0.956	250.00	0.004	0.999

Table 2 Isotherm parameters for Pb(II) adsorption on CCNC-nZVI

Temperature /K	Langmuir			Freundlich		
	q_{max} /(mg·g^{-1})	K_L/(L·mg^{-1})	R^2	K_F/(mg·g^{-1})	n	R^2
298.15	653.59	0.23	0.941	149.26	3.60	0.896
308.15	581.40	0.24	0.990	131.57	3.69	0.975
318.15	505.05	0.14	0.985	102.20	3.76	0.993

Table 3 Comparison of the maximum Pb(II) adsorption capacity on various adsorbents

Adsorbent	Initial pH	T/°C	Q_m /(mg·g^{-1})	Ref.
Amino-functionalized magnetic sludge-biochar	5.5	25	127.0	[39]
Hollow Fe_3O_4@PDA nanoparticles	5.0	25	57.25	[40]
Magnetite-decorated Si-Schiff base complex	5.0	25	133.64	[38]
Activated carbon supported zero-valent iron composite	6.0	25	59.35	[41]
Oxidized mesoporous carbon from asphalt and aluminum isopropoxide	6.5	30	277.8	[37]
Chitosan nanoparticle	5.0	25	94.34	[42]
Chitin nanofibers	5.0	25	60.24	[42]
Magnetic Fe_3O_4-mesporous magnesium silicate	5.0	43	247.5	[43]
Sepiolite-supported nanoscale zero-valent iron	6.0	28	44.05	[44]
Zero valent iron magnetic biochar composites	6.0	30	60.8	[45]
CCNC-nZVI	4.0	25	653.59	This work

layer [48]. Adsorption and co-precipitation of contaminants with iron oxides/hydroxides may represent another removal mechanism, suggesting that some new adsorption sites could be formed during the Pb(II) adsorption process. As shown in Fig. 6(e), the peaks appearing at 529.2, 530.8 and 532.3 eV could be attributed to oxide (O^{2-}), hydroxide (OH^-) and adsorbed water (H_2O), respectively [46]. It is also worth noting that the peaks at 529.2 and 530.8 eV were relatively weak (30.9%), indicating that the surface of the supported nZVI particles was mainly covered by adsorbed water [49]. On the other hand, the spectrum of CCNC-nZVI after Pb(II) adsorption (Fig. 6(f)) was well separated into signals at 529.7, 531.1 and 532.8 eV, and the area of peak at 529.7 and 531.1 eV was found to be increased by 62.2%. Compared with pre-adsorption, this result demonstrated that the relative content of O^{2-} and OH^- was significantly increased, further suggesting the formation of a large amount of FeOOH, $Fe(OH)_3$ and $Pb(OH)_2$, perfectly fitting the spectral data of Pb 4f and Fe 2p.

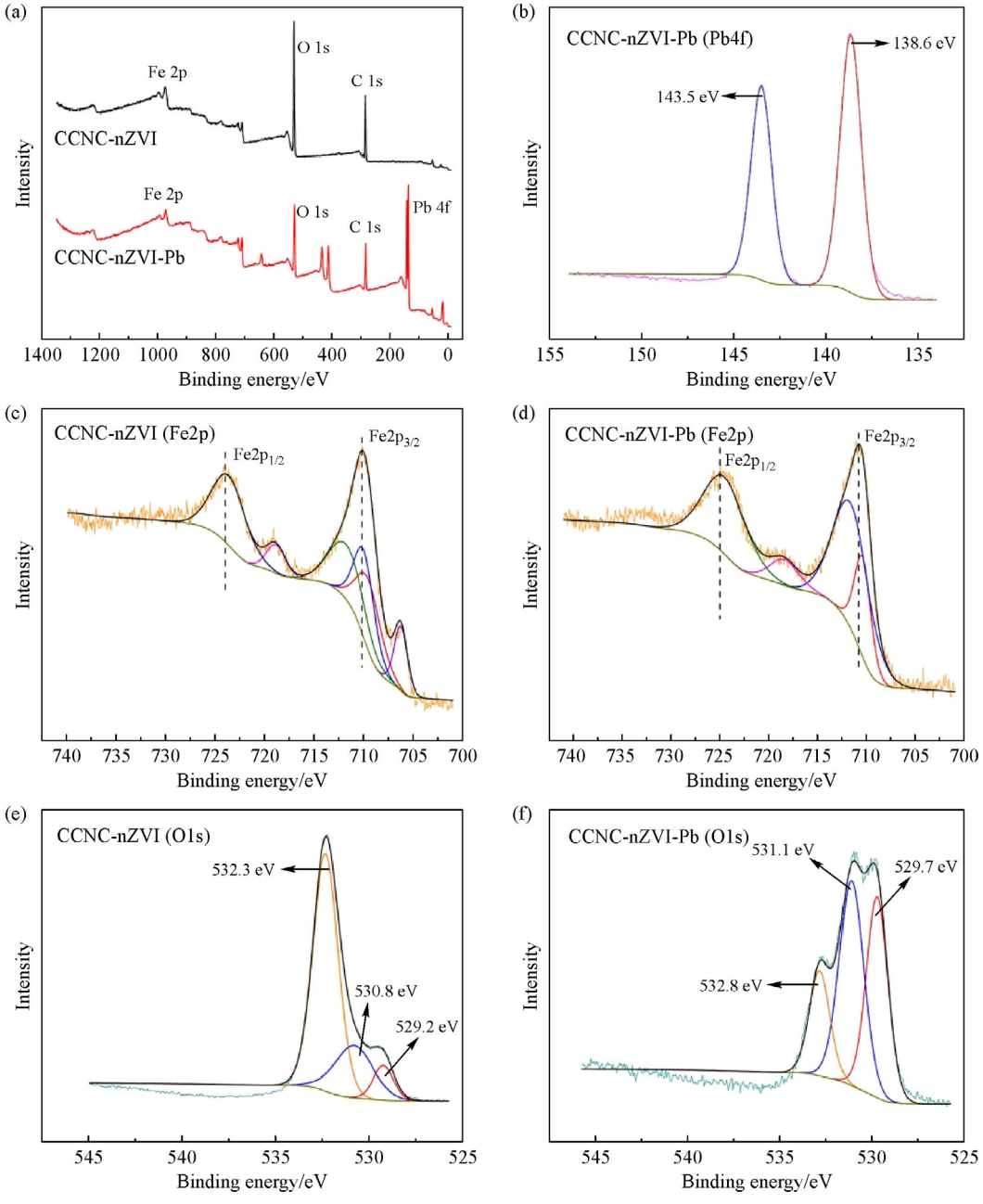

Fig. 6 (a) XPS full-scan surveys; (b) Pb 4f spectrum of CCNC-nZVI after Pb(II) adsorption; Fe 2p spectra of CCNC-nZVI (c) before and (d) after Pb(II) adsorption; O 1s spectra of CCNC-nZVI (e) before and (f) after Pb(II) adsorption.

4 Conclusions

In this study, CCNC, easily derived from the abundant and bio-renewable cellulose, was successfully used to immobilize nZVI. The resulting CCNC-nZVI composites with good distribution uniformity, high dispersity and resistance towards agglomeration and surface corrosion in aqueous solutions were synthesized via an *in-situ* reduction method. When used as adsorbents for heavy metal removal, CCNC-nZVI demonstrated excellent Pb(II) removal capabilities with an estimated adsorption capacity up to 653.59 $mg \cdot g^{-1}$ at 298.15 K, significantly higher than that of CCNC and frequently reported iron-based materials. Therefore, the as-synthesized CCNC-nZVI may represent an effective adsorbent material for heavy metal removal in future applications.

Acknowledgements This work was supported by the Key Planning Project of Science and Technology of Fujian Province, China (Grant No. 2018N0032). The authors declare no existing conflicts of interest.

Electronic Supplementary Material Supplementary material is available in the online version of this article at https://doi.org/10.1007/s11705-020-1924-y and is accessible for authorized users.

References

1. Ouni L, Ramazani A, Taghavi Fardood S. An overview of carbon nanotubes role in heavy metals removal from wastewater. Frontiers of Chemical Science and Engineering, 2019, 13(2): 274–295
2. Fu R B, Yang Y P, Xu Z, Zhang X, Guo X P, Bi D S. The removal of chromium (VI) and lead (II) from groundwater using sepiolite-supported nanoscale zero-valent iron (S-NZVI). Chemosphere, 2015, 138: 726–734
3. Chen B, Zhu C, Fei J, Jiang Y, Yin C, Su W, He X, Li Y, Chen Q, Ren Q, Chen Y. Reaction kinetics of phenols and *p*-nitrophenols in flowing aerated aqueous solutions generated by a discharge plasma jet. Journal of Hazardous Materials, 2019, 363: 55–63
4. Nahata M, Seo C Y, Krishnakumar P, Schwank J. New approaches to water purification for resource-constrained settings: Production of activated biochar by chemical activation with diammonium hydrogenphosphate. Frontiers of Chemical Science and Engineering, 2018, 12(1): 194–208
5. Yan Y, Huang P, Zhang H P. Preparation and characterization of novel carbon molecular sieve membrane/PSSF composite by pyrolysis method for toluene adsorption. Frontiers of Chemical Science and Engineering, 2019, 13(4): 772–783
6. Tao Q Q, Zhang X, Prabaharan K, Dai Y. Separation of cesium from wastewater with copper hexacyanoferrate film in an electrochemical system driven by microbial fuel cells. Bioresource Technology, 2019, 278: 456–459
7. Zhou R S, Zhou R W, Zhang X H, Bazaka K, Ostrikov K. Continuous flow removal of acid fuchsine by dielectric barrier discharge plasma water bed enhanced by activated carbon adsorption. Frontiers of Chemical Science and Engineering, 2019, 13(2): 340–349
8. Fu F L, Dionysiou D D, Liu H. The use of zero-valent iron for groundwater remediation and wastewater treatment: A review. Journal of Hazardous Materials, 2014, 267: 194–205
9. Yang F, Zhang S S, Sun Y Q, Cheng K, Li J S, Tsang D C W. Fabrication and characterization of hydrophilic corn stalk biochar-supported nanoscale zero-valent iron composites for efficient metal removal. Bioresource Technology, 2018, 265: 490–497
10. Cai Z Q, Fu J, Du P H, Zhao X, Hao X D, Liu W, Zhao D Y. Reduction of nitrobenzene in aqueous and soil phases using carboxymethyl cellulose stabilized zero-valent iron nanoparticles. Chemical Engineering Journal, 2018, 332: 227–236
11. Dhar P, Kumar A, Katiyar V. Fabrication of cellulose nanocrystal supported stable Fe(0) nanoparticles: A sustainable catalyst for dye reduction, organic conversion and chemo-magnetic propulsion. Cellulose (London, England), 2015, 22(6): 3755–3771
12. Zhao X, Liu W, Cai Z Q, Han B, Qian T W, Zhao D Y. An overview of preparation and applications of stabilized zero-valent iron nanoparticles for soil and groundwater remediation. Water Research, 2016, 100: 245–266
13. Mu Y, Jia F, Ai Z H, Zhang L Z. Iron oxide shell mediated environmental remediation properties of nano zero-valent iron. Environmental Science. Nano, 2017, 4(1): 27–45
14. Liu W, Tian S T, Zhao X, Xie W B, Gong Y Y, Zhao D Y. Application of stabilized nanoparticles for *in situ* remediation of metal-contaminated soil and groundwater: A critical review. Current Pollution Reports, 2015, 1(4): 280–291
15. Shi L N, Lin Y M, Zhang X, Chen Z L. Synthesis, characterization and kinetics of bentonite supported nZVI for the removal of Cr (VI) from aqueous solution. Chemical Engineering Journal, 2011, 171(2): 612–617
16. Horzum N, Demir M M, Nairat M, Shahwan T. Chitosan fiber-supported zero-valent iron nanoparticles as a novel sorbent for sequestration of inorganic arsenic. RSC Advances, 2013, 3(21): 7828–7837
17. Dong H R, Deng J M, Xie Y K, Zhang C, Jiang Z, Cheng Y J, Hou K J, Zeng G M. Stabilization of nanoscale zero-valent iron (nZVI) with modified biochar for Cr (VI) removal from aqueous solution. Journal of Hazardous Materials, 2017, 332: 79–86
18. Cai Z Q, Fu J, Du P H, Zhao X, Hao X D, Liu W, Zhao D Y. Reduction of nitrobenzene in aqueous and soil phases using carboxymethyl cellulose stabilized zero-valent iron nanoparticles. Chemical Engineering Journal, 2018, 332: 227–236
19. Lv X S, Xu J, Jiang G M, Xu X H. Removal of chromium (VI) from wastewater by nanoscale zero-valent iron particles supported on multiwalled carbon nanotubes. Chemosphere, 2011, 85(7): 1204–1209
20. Brinchi L, Cotana F, Fortunati E, Kenny J M. Production of nanocrystalline cellulose from lignocellulosic biomass: Technology and applications. Carbohydrate Polymers, 2013, 94(1): 154–169
21. Jiang S S, Daly H, Xiang H, Yan Y, Zhang H P, Hardacre C, Fan X L. Microwave-assisted catalyst-free hydrolysis of fibrous cellulose for deriving sugars and biochemical. Frontiers of Chemical Science and Engineering, 2019, 13(4): 718–726
22. Islam M S, Chen L, Sisler J, Tam K C. Cellulose nanocrystal (CNC)–inorganic hybrid systems: Synthesis, properties and applica-

tions. Journal of Materials Chemistry. B, Materials for Biology and Medicine, 2018, 6(6): 864–883

23. Maimaiti H, Awati A, Yisilamu G, Zhang D D, Wang S X. Synthesis and visible-light photocatalytic CO_2/H_2O reduction to methyl formate of TiO_2 nanoparticles coated by aminated cellulose. Applied Surface Science, 2019, 466: 535–544
24. Zarei S, Niad M, Raanaei H. The removal of mercury ion pollution by using Fe_3O_4-nanocellulose: Synthesis, characterizations and DFT studies. Journal of Hazardous Materials, 2018, 344: 258–273
25. Liu H, Song J, Shang S B, Song Z Q, Wang D. Cellulose nanocrystal/silver nanoparticle composites as bifunctional nanofillers within waterborne polyurethane. ACS Applied Materials & Interfaces, 2012, 4(5): 2413–2419
26. Chen L, Cao W J, Quinlan P J, Berry R M, Tam K C. Sustainable catalysts from gold-loaded polyamidoamine dendrimer-cellulose nanocrystals. ACS Sustainable Chemistry & Engineering, 2015, 3(5): 978–985
27. Cheng M, Qin Z Y, Chen Y Y, Liu J M, Ren Z C. Facile one-step extraction and oxidative carboxylation of cellulose nanocrystals through hydrothermal reaction by using mixed inorganic acids. Cellulose (London, England), 2017, 24(8): 3243–3254
28. Avila Ramirez J A, Fortunati E, Kenny J M, Torre L, Foresti M L. Simple citric acid-catalyzed surface esterification of cellulose nanocrystals. Carbohydrate Polymers, 2017, 157: 1358–1364
29. Lu J, Askeland P, Drzal L T. Surface modification of microfibrillated cellulose for epoxy composite applications. Polymer, 2008, 49(5): 1285–1296
30. Zhou C J, Wu Q L, Yue Y Y, Zhang Q G. Application of rod-shaped cellulose nanocrystals in polyacrylamide hydrogels. Journal of Colloid and Interface Science, 2011, 353(1): 116–123
31. Yu X L, Tong S R, Ge M F, Wu L Y, Zuo J C, Cao C Y, Song W G. Adsorption of heavy metal ions from aqueous solution by carboxylated cellulose nanocrystals. Journal of Environmental Sciences (China), 2013, 25(5): 933–943
32. Zhang X, Lin S, Chen Z L, Megharaj M, Naidu R. Kaolinite-supported nanoscale zero-valent iron for removal of Pb^{2+} from aqueous solution: Reactivity, characterization and mechanism. Water Research, 2011, 45(11): 3481–3488
33. Wu L M, Liao L B, Lv G C, Qin F X, He Y J, Wang X Y. Microelectrolysis of Cr (VI) in the nanoscale zero-valent iron loaded activated carbon. Journal of Hazardous Materials, 2013, 254-255: 277–283
34. Ling L, Pan B C, Zhang W X. Removal of selenium from water with nanoscale zero-valent iron: Mechanisms of intraparticle reduction of Se (IV). Water Research, 2015, 71: 274–281
35. Gong K D, Hu Q, Xiao Y Y, Cheng X, Liu H, Wang N, Qiu B, Guo Z H. Triple layered core-shell ZVI@carbon@polyaniline composite enhanced electron utilization in Cr(VI) reduction. Journal of Materials Chemistry. A, Materials for Energy and Sustainability, 2018, 6(24): 11119–11128
36. Su F C, Zhou H J, Zhang Y X, Wang G Z. Three-dimensional honeycomb-like structured zero-valent iron/chitosan composite foams for effective removal of inorganic arsenic in water. Journal of Colloid and Interface Science, 2016, 478: 421–429
37. Zhang X L, Lin Q L, Luo S Y, Ruan K Z, Peng K P. Preparation of novel oxidized mesoporous carbon with excellent adsorption performance for removal of malachite green and lead ion. Applied Surface Science, 2018, 442: 322–331
38. Khan A, Xing J, Elseman A M, Gu P C, Gul K, Ai Y J, Jehan R, Alsaedi A, Hayat T, Wang X K. A novel magnetite nanorod-decorated Si-Schiff base complex for efficient immobilization of U(VI) and Pb(II) from water solutions. Dalton Transactions (Cambridge, England), 2018, 43(33): 11327–11336
39. Huang X, Wei D, Zhang X W, Fan D W, Sun X, Du B, Wei Q. Synthesis of amino-functionalized magnetic aerobic granular sludge-biochar for Pb(II) removal: Adsorption performance and mechanism studies. Science of the Total Environment, 2019, 685: 681–689
40. Wang N, Yang D X, Wang X X, Yu S J, Wang H Q, Wen T, Song G, Yu Z M, Wang X K. Highly efficient Pb(II) and Cu(II) removal using hollow Fe_3O_4@PDA nanoparticles with excellent application capability and reusability. Inorganic Chemistry Frontiers, 2018, 5(9): 2174–2182
41. Liu X J, Lai D G, Wang Y. Performance of Pb(II) removal by an activated carbon supported nanoscale zero-valent iron composite at ultralow iron content. Journal of Hazardous Materials, 2019, 361: 37–48
42. Siahkamari M, Jamali A, Sabzevari A, Shakeri A. Removal of lead (II) ions from aqueous solutions using biocompatible polymeric nano-adsorbents: A comparative study. Carbohydrate Polymers, 2017, 157: 1180–1189
43. Zhao Z F, Zhang X, Zhou H J, Liu G, Kong M G, Wang G Z. Microwave-assisted synthesis of magnetic Fe_3O_4-mesoporous magnesium silicate core-shell composites for the removal of heavy metal ions. Microporous and Mesoporous Materials, 2017, 242: 50–58
44. Fu R B, Yang Y P, Xu Z, Zhang X, Guo X P, Bi D S. The removal of chromium (VI) and lead (II) from groundwater using sepiolite-supported nanoscale zero-valent iron (S-NZVI). Chemosphere, 2015, 138: 726–734
45. Rama Chandraiah M. Facile synthesis of zero valent iron magnetic biochar composites for Pb(II) removal from the aqueous medium. Alexandria Engineering Journal, 2016, 55: 619–625
46. Li X Q, Zhang W X. Equestration of metal cations with zerovalent iron nanoparticles—a study with high resolution X-ray photoelectron spectroscopy (HR-XPS). Journal of Physical Chemistry C, 2007, 111(19): 6939–6946
47. Abdel-Samad H W, Watson P R. An XPS study of the adsorption of chromate on goethite (α-FeOOH). Applied Surface Science, 1997, 108(3): 371–377
48. Noubactep C. A critical review on the process of contaminant removal in Fe^0-H_2O systems. Environmental Technology, 2008, 29(8): 909–920
49. Martin J E, Herzing A A, Yan W L, Li X Q, Koel B E, Kiely C J, Zhang W X. Determination of the oxide layer thickness in core-shell zerovalent iron nanoparticles. Langmuir, 2008, 24(8): 4329–4334